Mechanistic Insights into the Pressure-Induced Polymerization of Aryl/Perfluoroaryl Co-Crystals

Margaret C. Gerthoffer,[a] Bohan Xu,[b] Sikai Wu,[a] Jordan Cox,[c] Steven Huss,[a] Shalisa M. Oburn,[a] Steven A. Lopez,[c] Vincent H. Crespi,[a,b,d,e] John V. Badding,[a,b,d,e] and Elizabeth Elacqua*[a,d]

[a] *Department of Chemistry, The Pennsylvania State University, University Park, PA, 16802.*

[b] *Department of Physics, The Pennsylvania State University, University Park, PA, 16802.*

[c] *Department of Chemistry and Chemical Biology, Northeastern University, Boston, MA, 02115.*

[d] *Materials Research Institute, The Pennsylvania State University, University Park, PA, 16802.*

[e] *Department of Materials Science, The Pennsylvania State University, University Park, PA 16802.*

1. Co-Crystal Structures as Characterized by X-Ray Diffraction (XRD)

Table S1. Crystallographic Data Collection Parameters for ArOH:ArFCHO and ArCHO:ArFOH Co-Crystals

CCDC Deposition #	2098283	2098284
Abbreviated Denotation	ArOH:ArFCHO	ArCHO:ArFOH
Empirical Formula	$C_{13}H_7F_5O_2$	$C_{13}H_7F_5O_2$
Formula Weight	290.19	290.19
Temperature (K)	293(2)	273.15
Crystal System	monoclinic	triclinic
Space Group	$P2_1/n$	P-1
a/Å	6.3270(13)	5.9872(15)
b/Å	26.441(5)	7.934(2)
c/Å	7.0232(14)	13.242(3)
α/90°	90	105.378(4)
β/90°	95.01(3)	99.982(5)
γ/90°	90	94.446(4)
Volume/Å^3	1170.4(4)	592.3(3)
Z	4	2
ρ_{calc}g/cm^3	1.647	1.627
μ/mm^{-1}	0.163	0.161
Radiation MoK_α	$\lambda = 0.71073$	$\lambda = 0.71073$
2θ range for data collection/ °	3.08 to 57.11	3.256 to 56.616
Reflections collected	5773	4715
Independent reflections	2709 [R_{int}= 0.0995, R_{sigma}= 0.1164]	2702 [R_{int}= 0.0145, R_{sigma}= 0.0245]
Data/restraints/parameters	2709/0/181	2702/0/185
Goodness-of-fit on F^2	1.092	1.089
Final R indexes [I>=2σ (I)]	R_1= 0.0796, wR_2= 0.1880	R_1= 0.0410, wR_2= 0.1226
Final R indexes [all data]	R_1= 0.1479, wR_2= 0.2305	R_1= 0.0497, wR_2= 0.1359

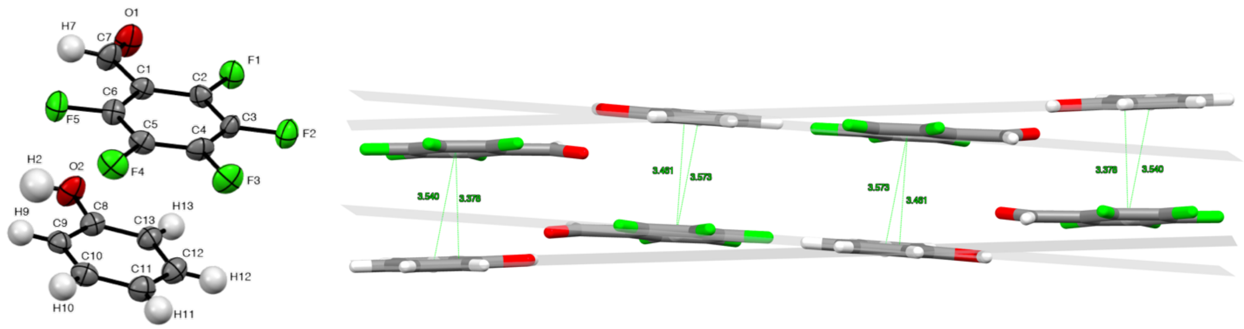

Figure S1. Diagram of the molecular structure generated by ORTEP with thermal ellipsoids set at 50% of the ArOH:ArFCHO co-crystal (left) and unit cell stacks of the co-crystal illustrated in Mercury (right).

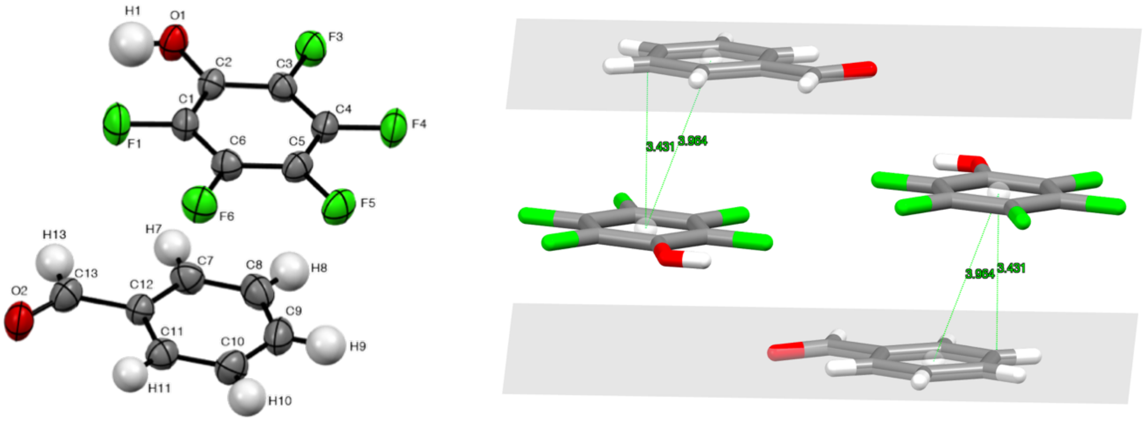

Figure S2. Diagram of the molecular structure generated by ORTEP with thermal ellipsoids set at 50% for the ArCHO:ArFOH co-crystal (left) and unit cell stacks of the co-crystal illustrate in Mercury (right).

Experimental X-Ray Collection: Methods

X-Ray Diffraction (XRD) was taken of the recovered solids to confirm co-crystal formation at ambient pressure on a Rigaku Microfocus Micromax 007 X-Ray Generator equipped with a Saturn 944+ CCD detector at 293 K. Structures were solved and refined using ShelXT[1] intrinsic phasing and ShelXL,[2] respectively, as integrated into the Olex2[3] graphical interface. Non-hydrogen atom identification was achieved with a difference Fourier map and was refined anisotropically. Hydrogen atoms were placed in calculated positions in Olex2. Refinement proceeded using isotropic thermal parameters. Experimental data confirmed that the cell info does not match the individual components (low temp. for low-melting solids;[4-6] benzaldehyde is an amorphous liquid).

Explanations of Distances Between π-Parallel Stacks

To calculate the distance between the parallel stacks, the software Mercury[7] was utilized to calculate ring planes and ring centroids. As previously expressed by Tang and Strobel,[8] d_c is defined as the distance between calculated centroid rings while d_p is the distance between calculated ring planes. d_p can be estimated by measuring the distance between one ring plane and the latter centroid, though no precise exact singular distance exists as the crystallographic planes are never perfectly parallel. The slippage angle (ϕ) is defined as the angle presented between parallel stacks and can be estimated from the angle between d_c and d_p; higher slippage angles theoretically contribute to less π orbital overlap. We exhibit the variability of d_p and respective ϕ as a result of the non-parallel crystallographic planes in **Table S2**, where we illustrate d_p from both the Ar plane to the ArF centroid and the ArF plane to the Ar centroid. We note that in comparison to compressed *para*-substituted Ar/ArF co-crystals[8] that both new co-crystals are in agreement with expected d_p/d_c ratios to lead to facile nanothread formation upon fast "flash" compressions. **Figure S3** illustrates example calculations for both ArOH:ArFCHO and ArCHO:ArFOH.

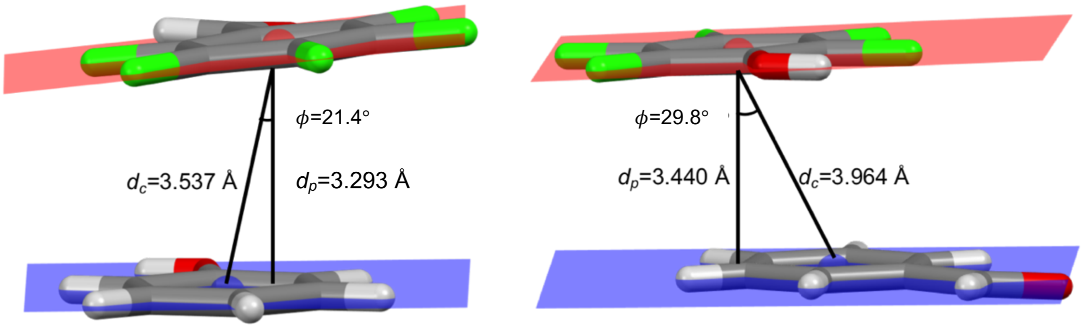

Figure S3: Examples of calculated centroid to centroid distances (d_c) and centroid to plane (d_p) distances in ArOH:ArFCHO (left) and ArCHO:ArFOH (right) stacks.

Table S2. Key Intermolecular Interactions within ArOH:ArFCHO and ArCHO:ArFOH Co-Crystals at Ambient Pressure, with respective slippage angles in parentheses.

	ArOH:ArFCHO	**ArCHO:ArFOH**
O···O Distance	2.788 Å	2.648 Å
Centroid to Centroid (d_c) #1	3.537 Å	3.964 Å
Centroid to Centroid (d_c) #2	3.575 Å	3.980 Å
#1: ArF Plane to Ar Centroid (d_p)	3.293 Å (21.4°)	3.440 Å (29.8°)
#1: Ar Plane to ArF Centroid (d_p)	3.242 Å (23.6°)	3.431 Å (30.1°)
#2: ArF Plane to Ar Centroid (d_p)	3.364 Å (22.9°)	3.393 Å (30.2°)
#2: Ar Plane to ArF Centroid (d_p)	3.463 Å (14.4°)	3.367 Å (32.2°)

2. Differential Scanning Calorimetry of ArOH:ArFCHO Co-Crystal

Due to the slightly higher R factor obtained for the crystal structure, additional evidence was sought to illustrate bulk co-crystallization. Differential scanning calorimetry (DSC) was thus acquired of each solid individual components and of the co-crysals as illustrated in **Figure S4**. DSC measurements were taken using a TA Instruments Q2000 DSC. Approximately 1 mg of solid sample was initially cooled to -60 °C from room temperature at a rate of 20 °C/min. The samples were then held at -60 °C for 5 minutes before being heating up to 80 °C at a rate of 10 °C/min. No phase transitions were observed for either the individual components or the co-crystal. An increase in the melting temperature for the co-crystal was observed compared to the individual components, alluding to the presence of enthalpically ordered intermolecular interactions.

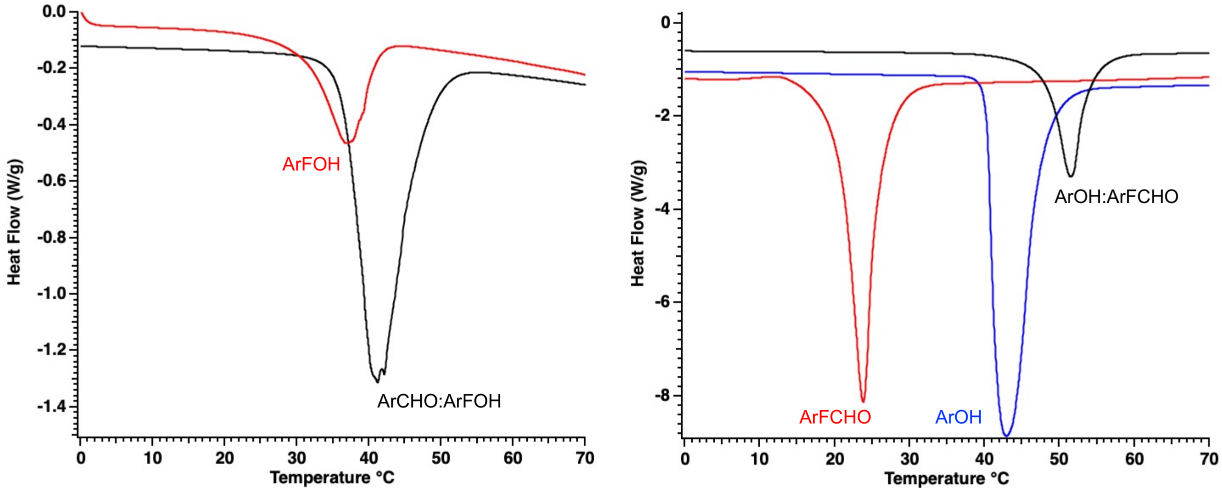

Figure S4: DSC traces ArCHO:ArFOH and components (left) and ArOH:ArFCHO and components (right), illustrating the prominent shift in melting point to a higher temperature in the co-crystalline solid. Co-crystal traces are black, perfluorinated species are red, and hydrogenated species are blue.

3. Hirshfeld Surface Area Calculation and Calculation of Void Space

Hirshfeld surfaces were calculated in the program CrystalExplorer17[9] using the input CIF files as noted above. Molecules under extreme pressures exhibit multiple stresses due to a reduction in available volume, often affording strange unfavorable intermolecular interactions. As a result, high-pressure phase transitions are often present in softer materials to minimize the steric encumbrance of limited space, despite oftentimes carefully engineered intermolecular interactions at ambient pressure. Using the Hirshfeld surface area model,[10] the amount of void space can be estimated to determine the availability of molecular movement after acquiring the volume encompassed by the surface area, which could lend insights into a molecule's capability of experiencing large pressure-induced phase changes. A calculation of the void space of the following co-crystals were performed by subtracting the total volume encompassed by the Hirshfeld surface in a unit cell by the total volume of the unit cell as obtained in single-crystal structure resolution. The void space available in conjunction with strong engineered intermolecular interactions may play a role in facilitating the future prediction of high-pressure phase transitions for facile templated nanothread formation.

Table S3. Calculation of Void Space from the Volume Occupied by each Ar/ArF pair

	Unit Cell Volume	**Ar/ArF Pairs per Cell**	**Hirshfeld Surface Area of Ar/ArF Pair**	**Volume Occupied of an Ar/ArF Pair**	**Total Occupied Volume per Unit Cell**	**Volume of Void Space**
ArOH ArFCHO	1170.44 Å^3	4	252.28 Å^2	287.71 Å^3	1150.84 Å^3	19.6 Å^3
ArCHO ArFOH	592.259 Å^3	2	261.28 Å^2	290.89 Å^3	581.78 Å^3	10.5 Å^3

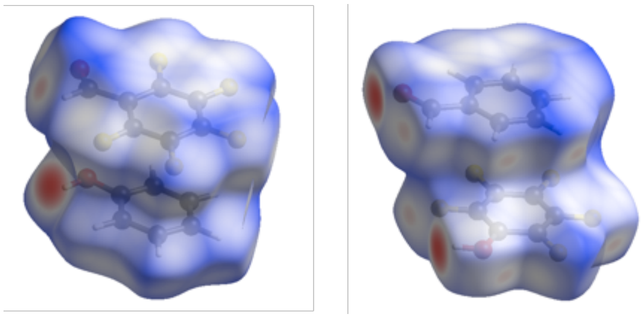

Figure S5: Calculated Hirshfeld surfaces of ArOH:ArFCHO (left) and ArCHO:ArFOH (right); red coloring features the location of the nearest closest contacts due to hydrogen bonds.

4. Theoretical Compressions: Unit Cell Changes upon Pressure Induction

As discussed in the main text, each experimentally acquired CIF file was subjected to pressure to elucidate the compressibility of each co-crystal. The relative decrease in unit cell axes are plotted in **Figure S6** for both co-crystals. As qualitatively noted, each axis decreases for both crystals when subjected to pressure. For the ArOH:ArFCHO co-crystal, the *b* axis compresses most significantly between 2 and 6 GPa, correlating likely to shortening of the hydrogen-bonding units; experimentally, this may result in greater stability for the co-crystal, as the already strong hydrogen bonds are strengthening. For the ArCHO:ArFOH co-crystal, both the *b* (π-π stacking) and *c* (hydrogen-bonding) axis compresses the most significantly within the same pressure range. Experimental correlation likely explains the desire for subtle phase changes, due to a more dramatic change in two of the main intermolecular interactions maintaining the structure of the solid. Also noted in **Figure S7** is the change in slippage angle upon pressure induction for both co-crystals, as correlated in **Table S2** to four non-symmetrically equivalent d_p stacks. For ArOH:ArFCHO, the slippage angle increases consistently for all non-symmetric stacks. For ARCHO:ArFOH, the slippage angle decreases along one stack and increases along another stack.

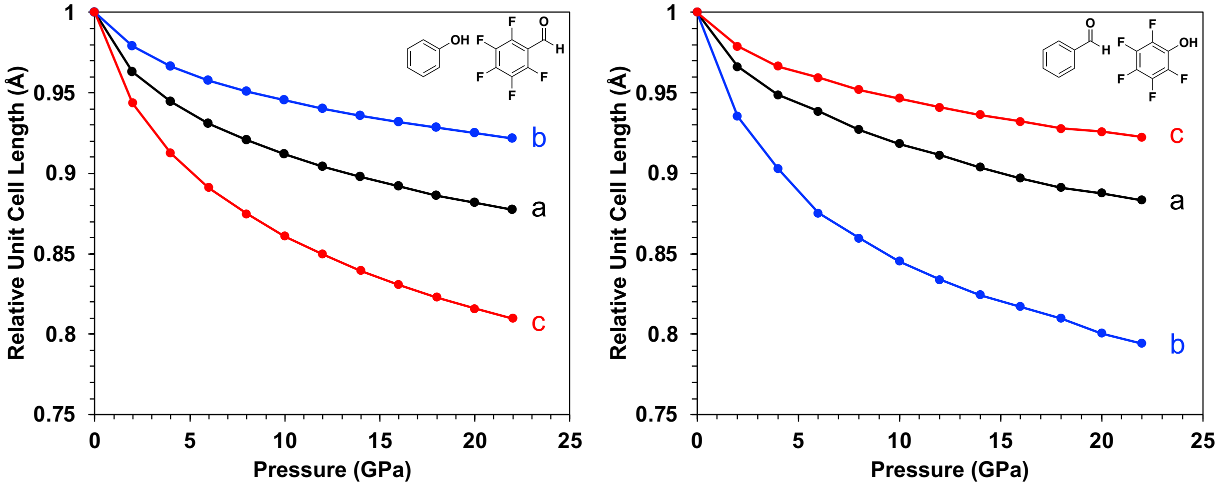

Figure S6: Relative change in unit cell lengths upon pressure induction for the *a*-axis (black), *b*-axis (blue), and *c*-axis (red) for the ArOH:ArFCHO (left) and ArCHO:ArFOH (right) co-crystals. The hydrogen-bonding axis is the most compressible axis for the ArOH:ArFCHO co-crystal, while the π-π stacking axis is most compressible for the ArCHO:ArFOH co-crystal.

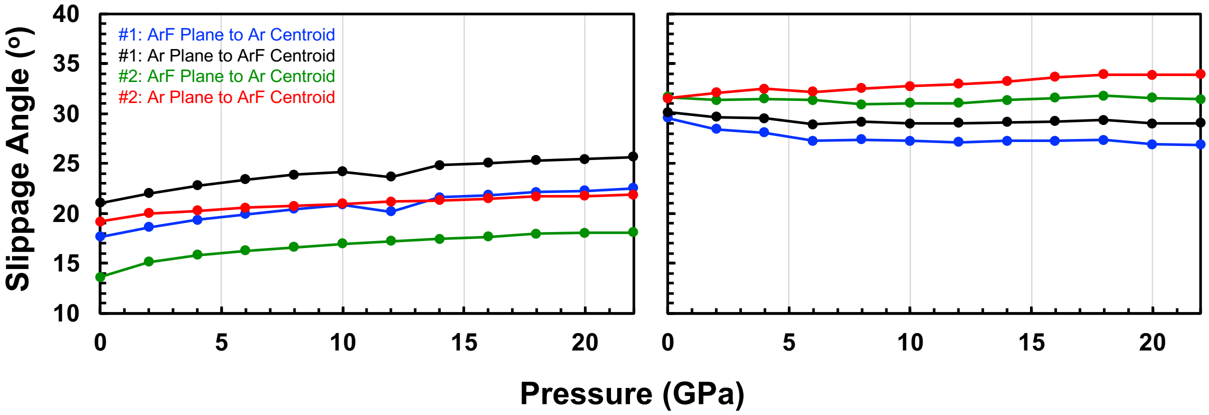

Figure S7. Slippage angle between Ar/ArF planes to Ar/ArF centroids upon pressure induction in the ArOH:ArFCHO co-crystal (left) and ArCHO:ArFOH co-crystal (right).

5. Vibrational Spectroscopy

Experimental Parameters

Raman spectra were collected every 2 to 3 GPa on compression/decompression on a Renishaw inVia Raman spectrometer equipped with a 633 nm laser excitation (2.3 mW power) and CCD detector. To focus on the sample through the diamonds, a 20× long-pass 0.35 NA objective was utilized in addition to a 5 μm pinhole to cut out additional light scattering from air. *In situ* pressure determinations were acquired from the fluorescence of a ruby chip.[11]

Co-crystals formed prior to compression were analysed using Attenuated Transmission Reflectance (ATR) spectroscopy using an FTIR Bruker Vertex V70 with an ATR attachment accessory. Transmission infrared (IR) spectroscopy was collected on samples recovered after slow compression as adhered in a DAC gasket using a Bruker Hyperion 3000 Microscope equipped with an MCT detector.

IR Spectroscopy Peak Assignments

IR spectroscopy was utilized prior to the compression of both co-crystals to study the co-crystallization behavior and subsequent vibrational signals changing as a result of prominent intermolecular interactions.[12,13] We compare here the peak shifts as a result of both compression (**Table S4**) and co-crystal formation (**Table S5, S6**) to elucidate key effects of each.

Table S4. IR Spectral Note: Keto-Enol Tautomerization Analysis Before and After Compression

	–OH Stretch	**C=O Stretch**	**C=O Intermol.**
ArOH:ArFCHO Before	3417	1691	1653; 1651; 1635
ArOH:ArFCHO After	3421 b	1708	1612; 1602; 1590
ArCHO:ArFOH Before	3097 b	1690	1597; 1582; 1662
ArOH:ArFCHO After	3393 b	1695	~1628

Table S5. Major IR Spectral Peak Assignments of ArOH:ArFCHO Co-Crystal Compared to Individual Components

Phenol	**Pentafluoro-benzaldehyde**	**Co-Crystal Before Compression**	**Peak Assignment**
3219 b	-	3415	Hydrogen bonded -OH stretching
-	-	-	Sp^3-hybridized stretching
3093; 3046; 3023	2912	3092; 3051	Sp^2-hybridized stretching
	2709	2958; 2929	C—H aldehyde stretching
	1704	1690	C=O stretching (conjugated)
1593	1651; 1635	1651; 1633; 1604; 1590	C=C stretching (conjugated, cyclic)
1498; 1472	1519; 1493	1521; 1492; 1468	C—H bending
-	1401	1426; 1403	C—H bending (aldehyde)
1370 (shoulder 1391; 1316; 1293	-	1353; 1318	O—H bending (phenol)
-	1309; 1273	1260; 1214	C—F stretching
1220 b; 1167; 1151	-	1171; 1147	C—O stretching
-	1150; 1127; 1090	1132 b,	C—F bending
1071; 1022		1071	C—O secondary alcohol stretching
999; 978; 962	1003	998	C=C bending, monosubstituted alkene
887	940	947	Tertiary C—(OH)
810	805	804	C—H bending, aromatic
745	725 w	758; 694	C—H disubstituted bending
686; 617; 532	629; 576	631; 576; 528	Aromatic derivatives/fingerprint

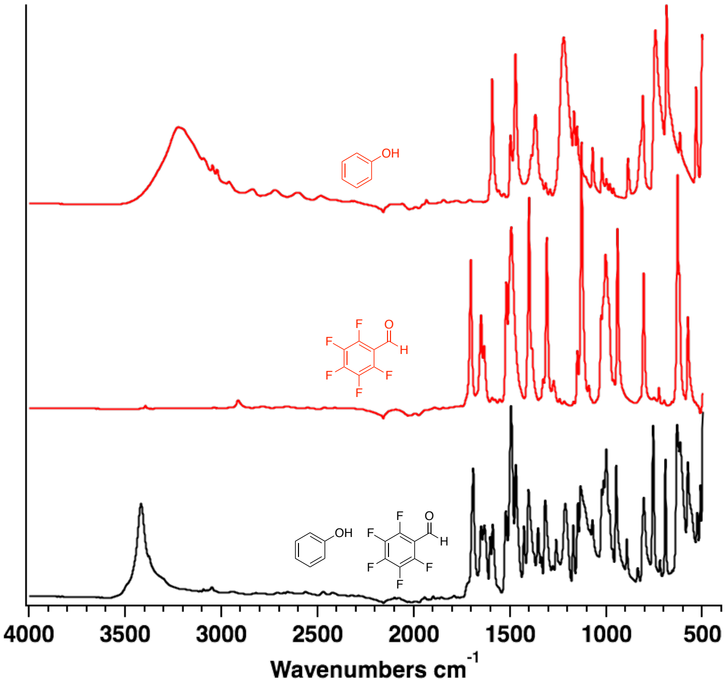

Figure S8: IR spectral overlay illustrating co-crystal formation as evidenced from distinctive vibrational shifts from the individual components phenol (red, top), pentafluorobenzaldehyde (red, middle) and ArOH:ArFCHO co-crystal (black).

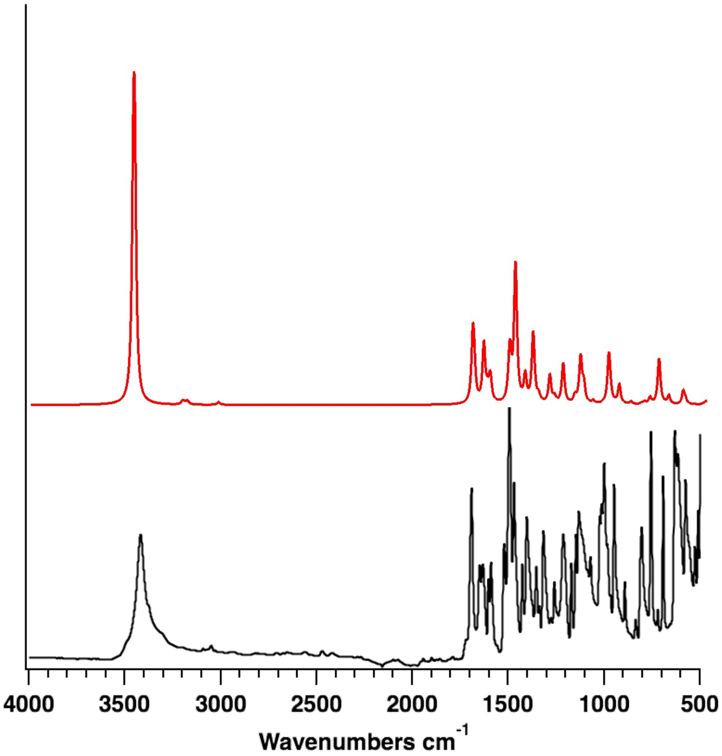

Figure S9: IR spectral overlay of precursor ArOH:ArFCHO co-crystal prior to compression (black) compared to theoretical vibrational shift prediction as simulated from .cif (red).

Table S6. Major IR Spectral Peak Assignments of ArCHO:ArFOH Co-Crystal Compared to Individual Components

Benzaldehyde	**Pentafluoro-phenol**	**Co-Crystal Before Compression**	**Peak Assignment**
-	3339	3096, b	H-bonded -OH stretching
-	-	-	Sp^3-hybridized stretching
3062; 3032	3022, 3006 w	b, w/ -OH	Sp^2-hybridized stretching
2934; 2827		2878	C—H aldehyde stretching
1699		1689; 1662	C=O stretching (conjugated)
1600; 1583	1516; 1483	1597; 1581	C=C stretching (conjugated, cyclic)
1493	1384; 1357 (phenol O-H); 1318	1532 (shoulder); 1514	C-H bending
1453; 1386 b		1455	C—H bending (aldehyde)
1311; 1272; 1205; 1172	1258; 1238	1401	O—H bending (phenol)
1100, 1071	1159	1343; 1316; 1293	C—F stretching
-	-	1255; 1236	C—O stretching
-	-	1210	C-F bending
-	1133	1173; 1156; 1132	C—O secondary alcohol stretching
1026	1023	1072	C=C bending, monosubstituted alkene
924, b	967	1014; 991; 972	Tertiary C-(OH)
829		833	C—H bending, aromatic
749	783	784; 750	C—H disubstituted bending
700; 649	650; 609	686; 655; 607; 559	Aromatic derivatives/fingerprint

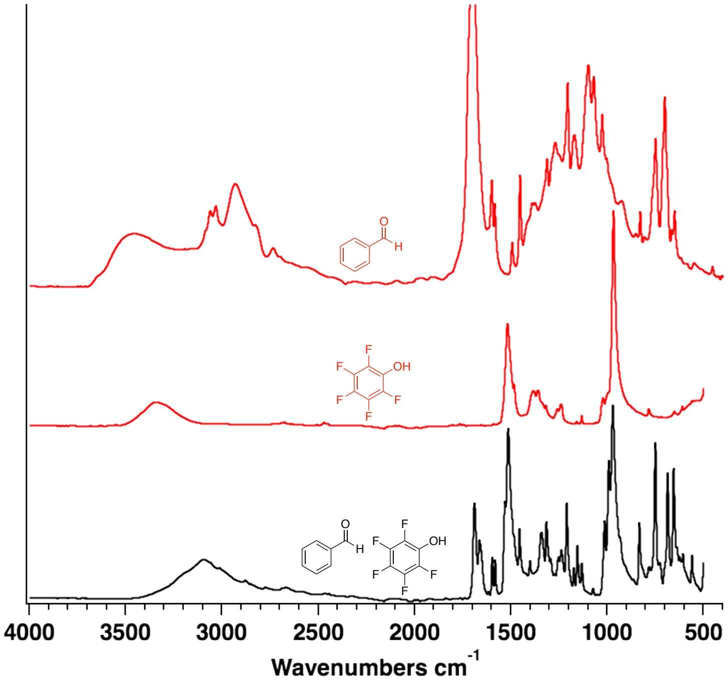

Figure S10: IR spectral overlay illustrating formation of the target ArCHO:ArFOH co-crystal (black) compared to individual components (benzaldehyde (red, top) and pentafluorophenol (red, middle)) Water and/or benzoic acid impurity is observed in as-purchased benzaldehyde and is removed upon co-crystallization. The broad peaks for both benzaldehyde and pentafluorophenol are characteristic for liquids and low-melting solids due to line broadening from Lorentzian and Gaussian distributions.[14,15,16]

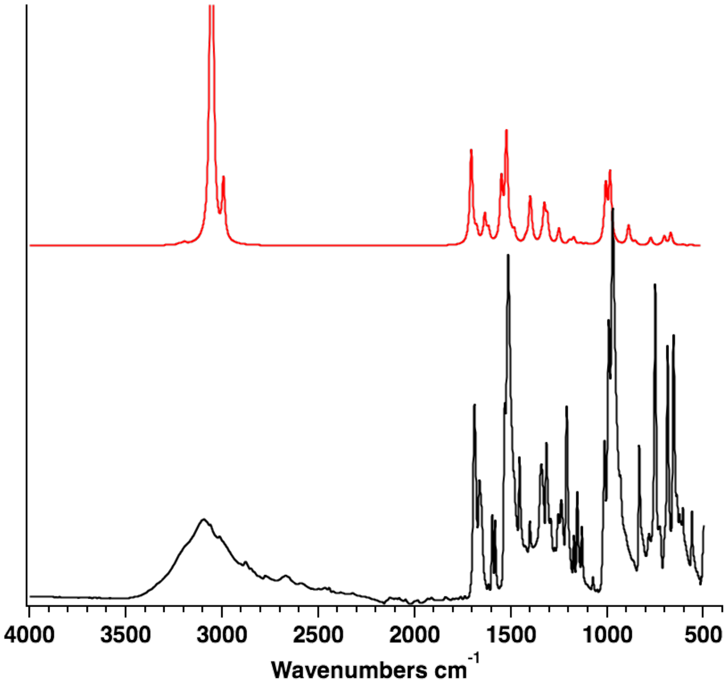

Figure S11: IR spectral overlay of precursor ArCHO:ArFOH co-crystal prior to compression (black) compared to theoretical vibrational shift prediction as simulated from .cif (red).

6. Microscopy and Recovered Synchrotron X-Ray Diffraction (XRD)

Recovered samples from DAC compressions as adhered in the gasket were analysed using an Olympus BX62 microscope, corrected with a blue-field collection plate and cross-polarizers for birefringence to indicate axial crystallinity. A 530 nm half waveplate was additionally used as specified to visually represent birefringence with more distinct colours.

Synchrotron radiation was utilized from the Advanced Photon Source (APS) at Argonne National Lab, beamline 16-BM-D, on recovered samples adhered in DAC gaskets. Scattering patterns were obtained from a 25 keV 5×5 µm micro-focused beam on a MAR345 area detector that rastered over a 50 μm^2 area while collecting a maximum ω angle of ±30° without obtaining major gasket diffraction. The software Dioptas[17] enabled data interpretation for 2D scattering images and 1D powder patterns. CrystalDiffract was utilized to simulate the powder diffraction of the ArCHO:ArFOH co-crystal and its thread products, based on the structures relaxed by DFT (see section 9 below).

7. X-Ray Photoelectron Spectroscopy (XPS)

XPS was conducted using a Physical Electronics VersaProbe II with a concentric hemispherical analyzer on recovered gasket samples about 40 microns in thickness. Monochromatic Al K X-ray sources with low-energy electrons less than 5 eV ensured charge neutralization on the surface. A take-off angle of 45 degrees to the sample surface ensured a sampling depth of 3 to 6 nm. The instrument was quantified with poly(vinylpyrrolidone) as a reference. Data was plotted using software casaXPS as illustrated in **Figures S12 and S13**.[18]

Previous reports of the compression of phenolic co-crystals have illustrated the possibility of keto-enol tautomerization on recovered samples. XPS has lent some insights into the possible reaction mechanism by looking at hybridization and relative carbon content of recovered gasket samples after compression. The high resolution C1s, O1s, and F1s spectrum are evidenced below in **Table S7, S8, and S9,** respectively, detailing the proposed concentration of each species predicted upon co-crystal recovery.

Likely some of the unconsumed benzaldehyde oxidized into benzoic acid after compression to achieve the resultant O-C=O functionality for the ArCHO:ArFOH co-crystal. This implies a minimum of 1.4% conversion of benzaldehyde into benzoic acid that can frequently occur upon exposure to air. With upwards of 38.3% of the carbon illustrating quantitative C-O hybridization, nucleophilic attack could occur onto the aldehyde's electropositive C=O. As XRD of the structure was solved before compression at ambient pressure, nucleophilic attack is likely occurring during the process of compression when under close solid-state confinement of overlapping functional groups. Rearrangement by nucleophilic attack could be evidenced from the CF_2 presence, illustrating that fluoride may be released during the pressure-induced polymerization.

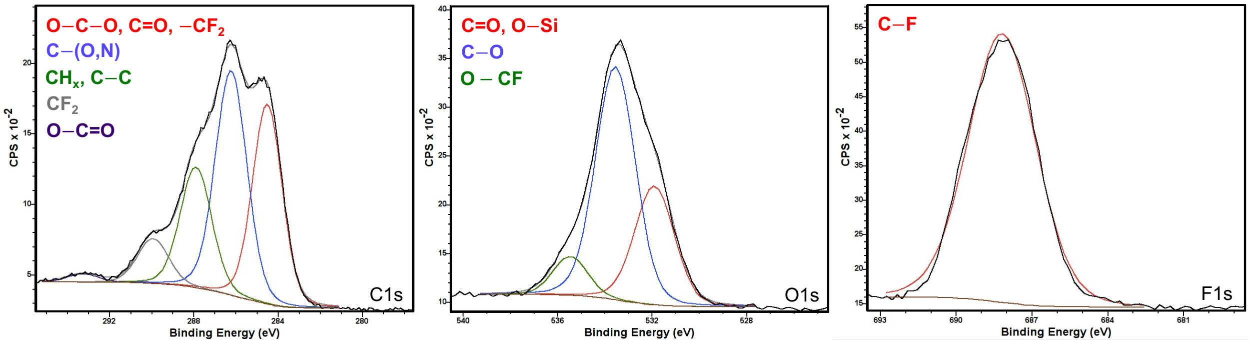

Figure S12. High Resolution C1s, O1s, and F1s spectrum of ArCHO:ArFOH

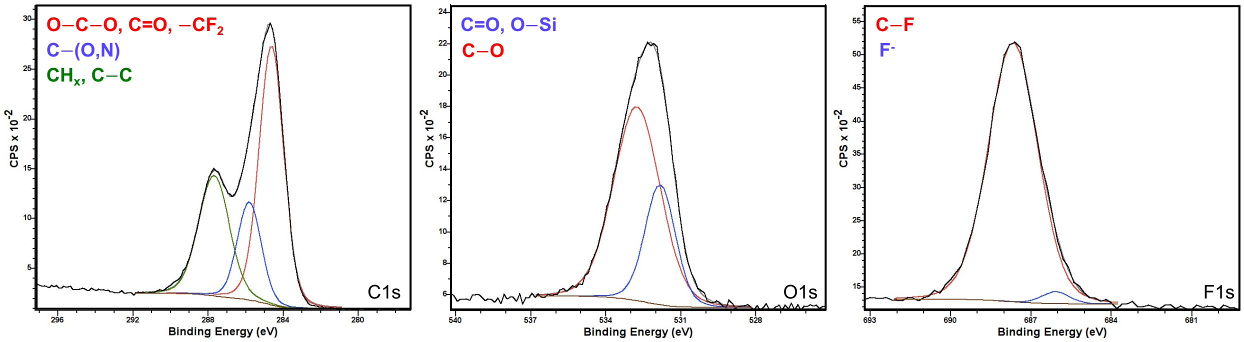

Figure S13. High Resolution C1s, O1s, and F1s spectrum of ArOH:ArFCHO

Table S7. High Resolution C1s XPS Spectrum

	CH_x, C—C	C—(O,N)	O—C—O, C=O, CF	$-CF_2$	-COO
ArCHO:ArFOH Experimental (%)	32.0	38.3	20.5	7.7	1.4
ArCHO:ArFOH Experimental (eV)	284.52	286.24	287.91	289.94	293.28
ArOH:ArFCHO Experimental (%)	51.0	18.9	30.1	0	0
ArOH:ArFCHO Experimental (eV)	284.63	285.79	287.69	-	-
ArOH ArFCHO Predicted (%)	46.1	7.7	46.1	0	0

Table S8. High Resolution O1s XPS Spectrum

	C—O	**C=O, O—Si**	**O—CF**	**O—C=O**
ArCHO:ArFOH Experimental (%)	60.4	30.8	8.8	0
ArCHO:ArFOH Experimental (eV)	531.92	533.56	535.47	-
ArOH:ArFCHO Experimental (%)	30.5	71.3	0	0
ArOH:ArFCHO Experimental (eV)	531.83	532.76	-	-
ArOH ArFCHO Prediction	50	50	0	0

Table S9. High Resolution F1s XPS Spectrum

	C—F	**F^-**
ArCHO:ArFOH Experimental (%)	100	0
ArCHO:ArFOH Experimental (eV)	688.1953	-
ArOH:ArFCHO Experimental (%)	97.4	2.6
ArOH:ArFCHO Experimental (eV)	687.67	686.09
ArOH ArFCHO Prediction	100	0

8. Dimer Barriers and Over-Compression of Co-Crystals

[4+2] cycloaddition thermal barriers were determined in the gas phase by density functional theory. Reactant dispersion-bound complexes, transition states, and product geometries were optimized with the M06-2X density functional and the 6-31+G(d,p) basis set in Gaussian 16. Stationary points were characterized as minima or transition states by vibrational frequency analysis. Reaction free energies were computed from thermochemical analysis at 298.15 K. Illustrated in **Figure S14** are the reactants chosen from ambient pressure crystal structure orientations, the transition state, and dimer product output for each molecule acting as the 4π component. The reactive atoms in each case were selected as those with the shortest interatomic C...C distances in the ambient pressure crystal structure. In the case of ArOH:ArFCHO, two sets of reactive atoms had similar interatomic distances and therefore a total of four transition states were optimized. The dimerization barrier was computed based on the transition state with the lowest free energy.

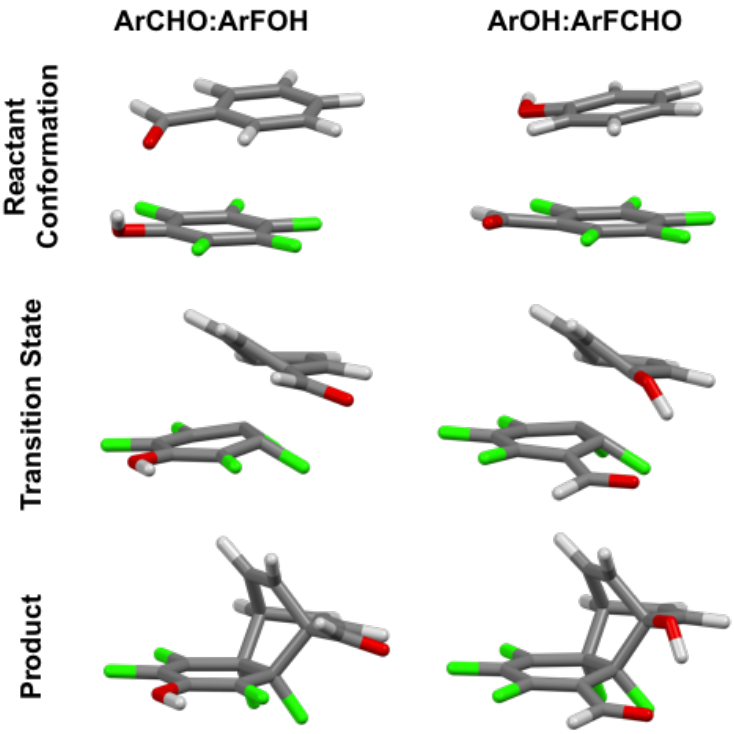

Figure S14. Illustrated are the reactant conformation, transition state, and dimer product for each of the co-crystals, ArCHO:ArFOH (left) and ArOH:ArFCHO (right).

To observe if reactivity is possible along a barrier-less pathway, over-compression was simulated up to 100 GPa to suggest that the ArCHO:ArFOH co-crystal has a higher likelihood of cross-linking the functional groups rather than reacting to form a sp^3 saturated backbone, likely due to the close-contacted functional groups. Over-compression of the ArOH:ArFCHO co-crystal to 100 GPa illustrates first the formation of an sp^3 saturated backbone followed by crosslinking.

9. Generation of Candidate Thread Packings of [4+2] Routes to ArCHO:ArFOH

DFT computations by Perdew-Burke-Ernzerhof (PBE)[19,20] exchange-correlation functional of general gradient approximation were completed using the software VASP.[21] The Projector Augmented Wave (PAW)[22] method with $1s^2$ electrons of C, F, O, being regarded as the core elections, was adopted. DFT-D3 with Becke-Jonason damping[23] is used as dispersion correction for structural relaxation. The energy cut-off is set to be 520 eV with a force convergence criteria of 0.01eV/Å. Gamma centred k meshes are implemented with step size smaller than 0.03 $Å^{-1}$ along any direction, for the co-crystal and reaction product relaxation. The k mesh step size is around 0.1 $Å^{-1}$ for the low-resolution flash ultra-high-pressure compression that aims to explore the polymerization pathway by theoretically compressing the co-crystal at 0 K to polymerization initiation at 100 GPa.

Super cells with dimensions greater than 9 Å, with k mesh step size around 0.05 $Å^{-1}$ were used to simulate the IR spectrum with a finite difference method.[24,25] The packages Phonopy[26] and Phonopy-Spectrum[27,28] were implemented to calculate phonon frequencies and IR spectrum. The simulated IR spectrum of Ar-CHO:ArF-OH co-crystal and thread products are rescaled by a factor of 1.03 to correlate with thermal differences in the experimental reactant's spectrum. This scaling factor, determined by comparing the spectrum of experimental co-crystal with that of the simulated co-crystal, is introduced to better predict the spectrum of the thread reaction products. This 3% rescaling is consistent with that generalized gradient approximations tend to underestimate phonon frequency by 3.6% on average.[29]

Candidate threads were formed composed of the two most likely [4+2] cycloaddition reactions based on the closest carbon-carbon contact distances (Thread 1 and Thread 2) from the structure solved at ambient pressure and relaxed (**Figure S15**). Due to the presence by XPS of the potential for carboxylic acid functionality, a thread was generated in which the aldehyde functionality was oxidized along the backbone (thread 4). The IR of all individual threads (**Figure S16**) and of their resultant relaxed packing (**Figure S17**) were generated for comparison to experimentally obtained spectra. The poor match of Thread 4 to the experimentally determined structures illustrates that aldehyde functionality is likely preserved along the backbone, with the recovered co-crystal comprising of the oxidation of benzaldehyde into benzoic acid upon exposure to air.

In the generation of the candidate thread structures, we note that the aldehyde (or carboxylic acid) and hydroxyl groups are gauche along the thread backbone, which likely prohibits steric bulk from gatekeeping a polymerization pathway. Moreover, each group is eclipsed with itself, two units down the backbone structure. Close hydrogen-bonding between the hydroxy and aldehyde is illustrated within the thread for Thread 1 but are slightly more distant for Thread 2.

From the packing of the threads, we note that both Thread 1 and 2 illustrate hydrogen-bonding patterns in which they dimerize with their nearest neighbor. As discussed in the main text, the purpose of generating the packing of these candidate structures was to illustrate the effects of intermolecular interactions on the theoretical vibrational spectra. We thus note that Thread 1 generates the closest vibrational frequencies to the acquired experimental spectra. Although this work does not feature an exhaustive list of candidate structures, we do note here the key importance of intermolecular interactions while installing pendant functional groups along a thread-like backbone.

An additional thread structure (Thread 3) was calculated by placing the functional groups *para* to one another along the thread backbone (**Figure S15**). This structure was generated to try and alleviate intermolecular interactions within the thread. Simulations of the IR of this thread exhibit a drastically different IR shift of the –OH bond than exhibited experimentally as illustrated in the main text. Furthermore, the O-H frequency of isolated ArFOH precursor molecule is computed to be 3684 cm^{-1}, and the C=O frequency of isolated ArCHO is computed to be 1708 cm^{-1}. They are close to the corresponding frequency of Thread 4, which are 3680 and 1754 cm^{-1}. This shows the change of hybridization by itself is not the main reason of the observed O-H frequency shift around 400 cm^{-1}.

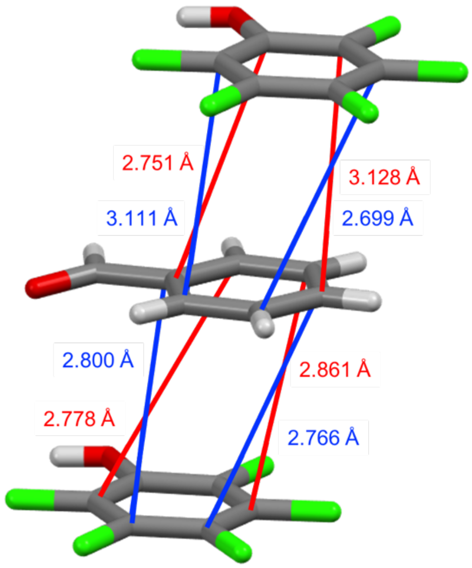

Figure S15. Nearest carbon-carbon contact distances in precursor thread structure. The closest distance was used as the most likely [4+2] cycloaddition initiation point to generate Thread 1 (blue), while the furthest distance was used to generate Thread 2 (red).

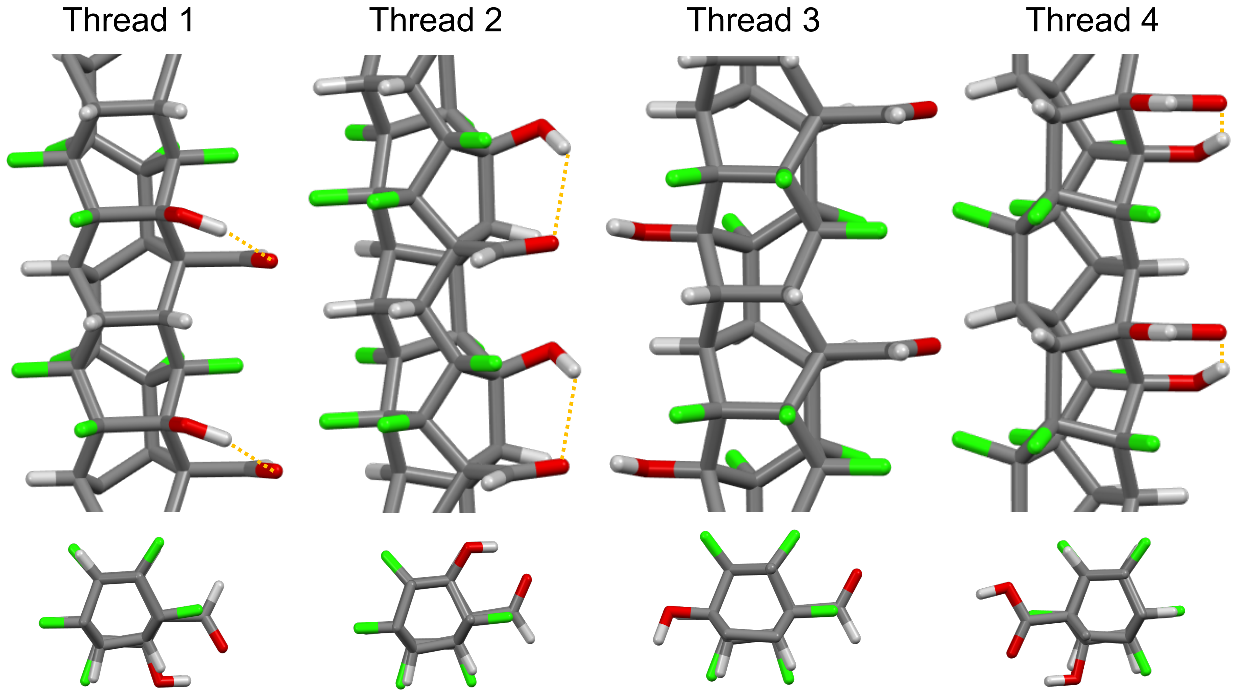

Figure S16. Candidate thread generation [4+2] cycloadditions, generated upon connectivity of the closest C-C contact distance (Thread 1, far left) and furthest C-C contact distance (Thread 2, middle left). Functional groups designed substituted *para* along the thread structure simulated threads without prevalent intermolecular interactions as labelled on Thread 3 (middle right). Replacement of the aldehyde functionalities with a carboxylic acid generated Thread 4 (far right). A "top-down" view is illustrated along the bottom.

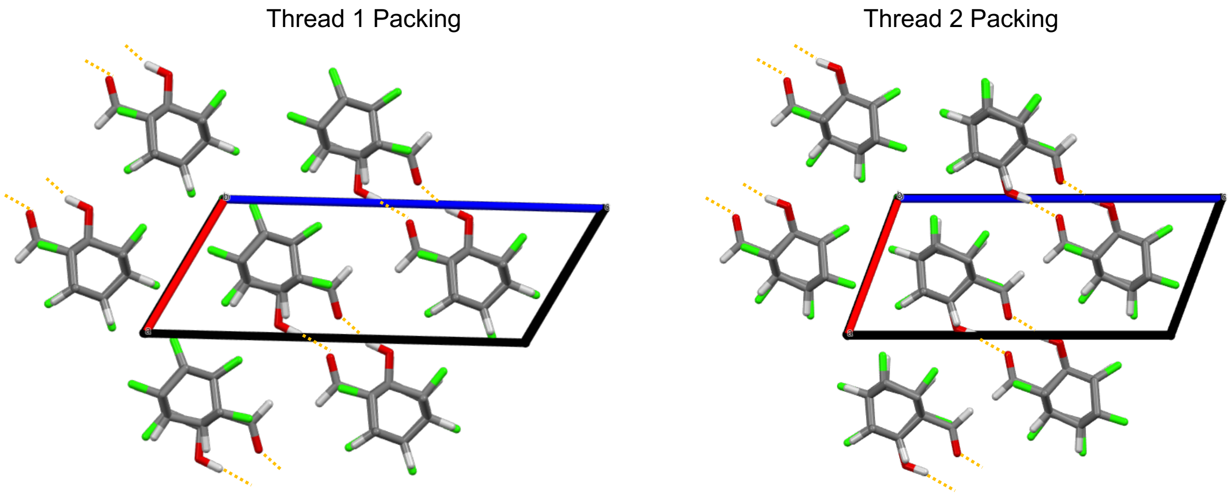
Thread 1 Packing

Thread 2 Packing

Figure S17. Packing of thread candidates generated by cycloadditions, looking down the *b* axis.

Our experiments suggest that even carefully engineered stacks of co-crystal can potentially result in unexpected high pressure phase changes to promote/prevent polymerization due to steric hindrance, geometrical bulk, and closely coordinated functional groups under extreme solid-state conditions.

REFERENCES:

1. Sheldrick, G.M. *Acta Crystallogr. A* **2008**, *64*, 112.
2. Sheldrick, G.M. *Acta Crystallogr. C* **2015**, *71*, 3.
3. Dolomanov, O.V.; Bourhis, L.J.; Gildea, R.J.; Howard, J.A.K.; Puschmann, H.J. *Appl. Crystallogr.* **2009**, *42*, 339-341.
4. Allan, D.R.; Clark, S.J.; Dwason, A.; McGregor, P.A.; Parsons, S. *Acta Crystallogr. B* **2002**, *58*, 1018-1024.
5. Das, D.; Banerjee, R.; Mondal, R.; Howard, J.A.K.; Boese, R.; Desiraju, G.R. *Chem. Comm.* **2006**, *5*, 555-557.
6. Paul, M.; Sudkaow, P.; Wessels, A.; Schlörer, N.E.; Neudörlf, J.-M.; Berkessel, A. *Angew. Chem. Int. Ed.* **2018**, *57*, 8310-8315.
7. Macrae, C.F.; Sovago, I.; Cottrell, S.J.; Galek, P.T.A.; McCabe, P.; Pidcock, E.; Platings, M.; Shields, G.P.; Stevens, J.S.; Towler M.; Wood, P.A. *J. Appl. Cryst.*, **2020**, *53*, 226-235.
8. Tang, W.S.; Strobel, T.A. *J. Phys. Chem. C* **2020**, *45*, 25062–25070.
9. Turner, M. J.; McKinnon, J. J.; Wolff, S. K.; Grimwood, D. J.; Spackman, P. R.; Jayatilaka, D.; Spackman, M. A. **2017** University of Western Australia http://hirshfeldsurface.net
10. Spackman, M.A.; Jayatilaka, D. *CrystEngComm*, **2009**, *11*, 19-32.
11. Shen G.; Wang Y.; Dewaele A.; Wu, C.; Frantanduono, D.E.; Eggert, J.; Klotz, S.; Dziubek, K.F.; Loueyre, P.; Fat'yanov, O.V.; Asimow, P.D.; Mashimo, T.; Wentzcovitch, R.M.M. et. al. *High Pres. Res.* **2020**, *40*, 299-314.
12. Biorad Raman Spectral Databases. http://bio-rad.com (accessed Jun. 20, 2021).
13. Elbagerma, M.A.; Edwards, H.G.M.; Munshi, T.; Hargreaves, M.D.; Matousek, P.; Scowen, I.J. *Cryst. Growth Des.* 2**010**, *10*, 2360-2371.
14. P. Pelikán, M. Ceppan, and M. Liška, *Applications of Numerical Methods in Molecular Spectroscopy* (Boca Raton, CRC Press, 1993), Chapter 2.

15. Sigma Aldrich Pentafluorophenol Spectrum https://www.sigmaaldrich.com/deepweb/assets/sigmaaldrich/quality/spectra/245/814/FTIR000073.pdf (accessed Dec. 12, 2021).
16. NIST Webbook Benzaldehyde Spectrum https://webbook.nist.gov/cgi/cbook.cgi?ID=C100527&Type=IR-SPEC&Index=2 (accessed Dec. 12, 2021).
17. Prescher, C.; Prakapenka, V.B. *High Press. Res.* **2015,** 35, 223–230.
18. Fairley N.; Fernandez, V.; Richard-Plouet, M.; Guillot-Deudon, C.; Walton, J.; Smith, E.; Flahaut, D.; Greiner, M.; Biesinger, M.; Tougaard, S.; Morgan, D. *Appl. Surf. Sci. Adv.* **2021**, 5, 100112.
19. Perdew, J.P.; Ernzerhof, M.; Burke, K. *J. Chem. Phys.* **1996**, *105*, 9982-9985.
20. Perdew, J.P.; Burke, K.; Ernzerhof, M. *Phys. Rev. Lett.* **1996**, *77*, 3865-3868.
21. Kresse, G.; Hafner, J. *Phys. Rev. B* **1993**, *47*, 558; ibid. **1994**, *49*, 14251.
22. Kresse, G.; Joubert, D. *Phys. Rev.* **1999**, *59*, 1758.
23. Grimme, S.; Ehrlich, S.; Goerigk, L. *J. Comp. Chem.* **2011**, *32*, 1456.
24. Parlinski, K.; Li, Z.Q.; Kawazoe, Y. *Phys. Rev. Lett.* **1997**, *78*, 4063.
25. Chaput, L.; Togo, A.; Tanaka, I.; Hug, G. *Phys. Rev. B* **2011**, *84*, 094302.
26. Togo, A.; Tanaka, I. *Scr. Mater.* **2015**, *108*, 1-5.
27. Kelton, J.M.; Burton, L.A.; Jackson, A.J.; Oba, F.; Parker, S.C.; Walsh, A. *Phys. Chem. Chem. Phys.* **2017**, *19*, 12452.
28. Phonopy Spectroscopy. http://github.com/JMSkelton/Phonopy-Spectroscopy/ (accessed Aug. 3, 2021).
29. He, L. et al. *Phys. Rev. B* **2014**, *89*, 064305.